Nature of Li$_2$O$_2$ Oxidation in a Li−O$_2$ Battery Revealed by Operando X-ray Diffraction

Swapna Ganapathy,[†] Brian D. Adams,[‡] Georgiana Stenou,[†] Maria S. Anastasaki,[†] Kees Goubitz,[†] Xue-Fei Miao,[†] Linda F. Nazar,*[,‡] and Marnix Wagemaker*[,†]

[†]Fundamental Aspects of Materials and Energy, Department of Radiation Science and Technology, Faculty of Applied Sciences, Delft University of Technology, Mekelweg 15, 2629 JB, Delft, The Netherlands

[‡]Department of Chemistry and the Waterloo Institute for Nanotechnology, University of Waterloo, Waterloo, Ontario N2L 3G1, Canada

🄢 *Supporting Information*

ABSTRACT: Fundamental research into the Li−O$_2$ battery system has gone into high gear, gaining momentum because of its very high theoretical specific energy. Much progress has been made toward understanding the discharge mechanism, but the mechanism of the oxygen evolution reaction (OER) on charge (i.e., oxidation) remains less understood. Here, using operando X-ray diffraction, we show that oxidation of electrochemically generated Li$_2$O$_2$ occurs in two stages, but in one step for bulk crystalline (commercial) Li$_2$O$_2$, revealing a fundamental difference in the OER process depending on the nature of the peroxide. For electrochemically generated Li$_2$O$_2$, oxidation proceeds first through a noncrystalline lithium peroxide component, followed at higher potential by the crystalline peroxide via a Li deficient solid solution (Li$_{2−x}$O$_2$) phase. Anisotropic broadening of the X-ray Li$_2$O$_2$ reflections confirms a platelet crystallite shape. On the basis of the evolution of the broadening during charge, we speculate that the toroid particles are deconstructed one platelet at a time, starting with the smallest sizes that expose more peroxide surface. In the case of in situ charged bulk crystalline Li$_2$O$_2$, the Li vacancies preferentially form on the interlayer position (Li1), which is supported by first-principle calculations and consistent with their lower energy compared to those located next to oxygen (Li2). The small actively oxidizing fraction results in a gradual reduction of the Li$_2$O$_2$ crystallites. The fundamental insight gained in the OER charge mechanism and its relation to the nature of the Li$_2$O$_2$ particles is essential for the design of future electrodes with lower overpotentials, one of the key challenges for high performance Li−air batteries.
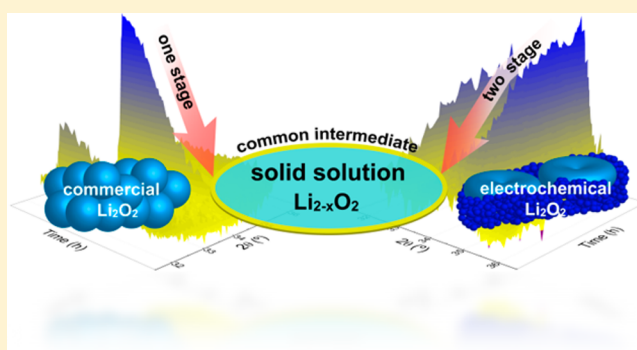
■ INTRODUCTION

Research into nonaqueous Li−air/Li−O$_2$[1,2] batteries has exploded over the past few years.[3−5] This is primarily due to their high theoretical specific energy in the charged state (∼11 500 W h/kg),[6] making them extremely attractive for electric automobiles. The electrochemical processes that drive this battery are represented by the total chemical reaction 2Li + O$_2$ ⇄ Li$_2$O$_2$. Several bottlenecks that impede the functioning of this battery system need to be addressed before it can become viable. These include the high (dis)charge overpotential resulting in a lower round trip efficiency,[2,7,8] slow kinetics, electrolyte instability (side product formation)[9−12] leading to poor cyclability, and the requirement of high purity O$_2$. Of fundamental importance is the understanding of the mechanism of lithium peroxide formation and oxidation and the governing factors. Over the past years there has been significant progress in the understanding of the Li$_2$O$_2$ formation process during discharge. Clear correlations have been established between the solvent donor number,[13] discharge voltage, current density,[14,15] and composition of the gas diffusion electrode on

the morphology of Li$_2$O$_2$ formed and the mechanism of their formation, be it via solution[14] or on the electrode surface.[10] But one of the many challenges of the Li−O$_2$ system includes the mechanism of Li$_2$O$_2$ oxidation which remains less well understood, with the elusive LiO$_2$ superoxide intermediate remaining experimentally very difficult to observe. There are only a few inconclusive reports of superoxide observation both in situ and ex situ.[15−17] Modeling approaches suggest a Li deficiency driven solid solution reaction resulting in the formation of Li$_{2−x}$O$_2$[18] or that smaller crystallites would decompose first at lower potentials.[19] Experimentally, it has been suggested that amorphous Li$_2$O$_2$ decomposes first at lower potentials[20] whereas a solid solution reaction has not been observed.

In this article, we combine operando X-ray diffraction (XRD), Rietveld refinement, calculations, and online electrochemical mass spectrometry (OEMS) to elucidate the
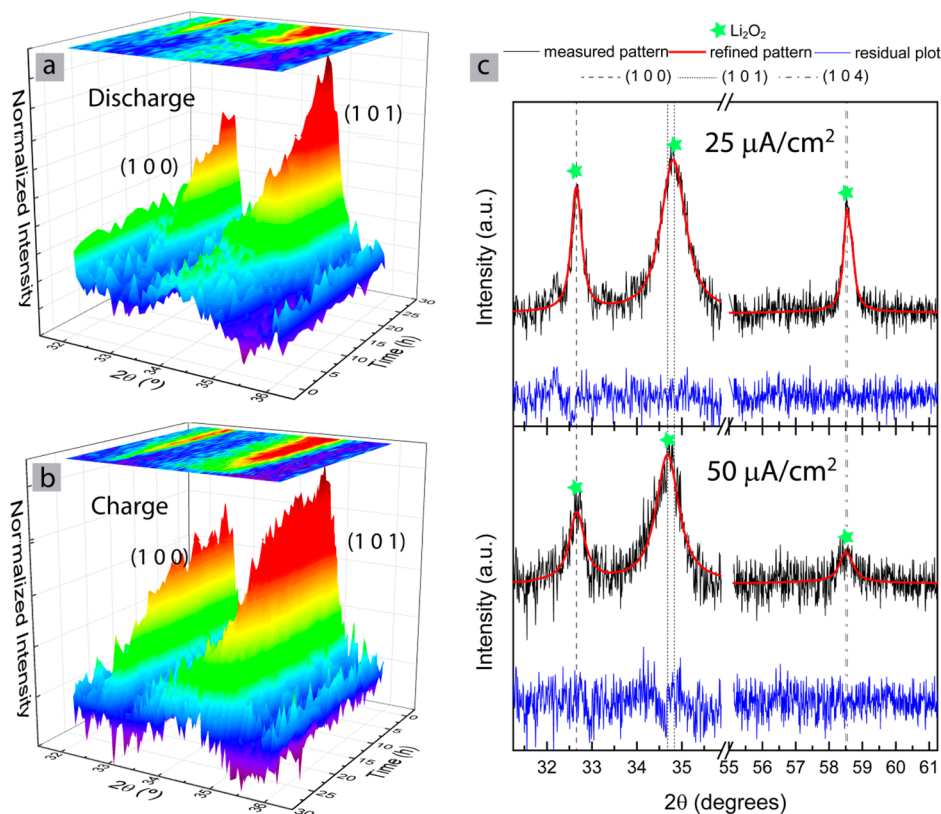
Figure 1. (a, b) Three dimensional discharge and charge plots of the XRD patterns in the 2θ region of $32-36°$, recorded operando as a function of time of Li_2O_2 with a constant current of $50\ \mu A/cm^2$. (c) Background subtracted diffraction patterns recorded operando after full discharge of the Li–O_2 cell and their Rietveld refinement with an R_{wp} of less than 2%. Differences in peak positions corresponding to the (1 0 1) and (1 0 4) reflections for the E-Li_2O_2 produced at current densities of 25 and 50 $\mu A/cm^2$, respectively, are indicated.

mechanism of the oxidation evolution reaction, comparing electrochemically generated Li_2O_2 (E-Li_2O_2) and bulk crystalline (commercial) Li_2O_2 (C-Li_2O_2) during the charge reaction in a Li–O_2 cell. A clear difference is observed between the oxidation of E-Li_2O_2 and C-Li_2O_2 which can be explained by the difference in the nature of the particles and crystallites. The OER mechanism, however, appears similar for both E-Li_2O_2 and C-Li_2O_2, as Rietveld refinement of the operando data reveals Li deficiency in both cases indicating that the OER takes place via a solid solution reaction.

■ MATERIALS AND METHODS

Operando XRD Cell. A Li–O_2 cell that allows X-ray diffraction measurements to be conducted in reflection mode during battery cycling was designed and custom built. The top half of the cell comprises a Kapton window with a diameter of 20 mm enclosed in a stainless steel casing with a small inlet to allow the intake of O_2 gas. An Al mesh current collector was integrated into this top half. The bottom half consisted of a stainless steel coin attached to a spring, also enclosed in stainless steel, akin to that of a typical Swagelok cell design. This formed the current collector on the anode side. The top and bottom halves of the cell were separated with a Teflon spacer to prevent a short circuit, after which they were clamped together from the outside with a nonconductive clamp. The battery stack was assembled within, with the cathode on the side of the Kapton window. The schematic is shown in the Supporting Information section (Figure S1).

Electrochemistry. Gas diffusion electrodes (cathodes) were fabricated by casting a mixture of activated carbon (Kuraray Chemical) and a lithiated Nafion binder[14,21] on carbon paper (Spectracarb). The cathodes were dried at 100 °C for 24 h to remove all surface adsorbed water, after which disks of 16 mm were punched from the sheets. The

preloaded Li_2O_2 cathodes were made by combining Vulcan XC72 carbon (Cabot Corp.), Li_2O_2 (Sigma-Aldrich, 90%), and PTFE with a weight ratio of 4:1:1 in 2-propanol and casting the mixture on Toray carbon paper (TGP-H-030, Fuel Cell Store). This was carried out in an argon filled glovebox (H_2O and O_2 content of <1 ppm). These preloaded Li_2O_2 electrodes were dried under vacuum at room temperature to remove the 2-propanol solvent. The electrolyte consisted of a solution of 1 M lithium bis(trifluoromethanesulfonyl)-imide (LiTFSI, Aldrich) dissolved in dried and distilled tetraethylene glycol dimethyl ether (TEGDME, <1 ppm of H_2O). The battery, comprising the cathode, a glass microfiber separator (Whatman) soaked with the electrolyte, and a Li-metal anode, was assembled in the previously described operando XRD cell in the glovebox. The cell was subsequently connected to O_2 (Linde, 99.995%) under a pressure of 1.5 bar where it was allowed to equilibrate for between 2 and 6 h before it was tested. Electrochemical (dis)charge tests were performed with a MACCOR 5300 battery cycler.

XRD Measurements. X-ray diffraction measurements were performed on a PANalytical X'Pert Pro PW3040/60 diffractometer with Cu Kα radiation operating at 45 kV and 40 mA in an angular 2θ range of $31-66/71°$. Scans of 1 h and 7 min each were recorded for the batteries that underwent a complete (dis)charge cycle and of 30 min each for batteries that contained the pre-Li_2O_2 loaded cathodes that underwent charge only. Refinement of the diffraction data was carried out using the Rietveld method as implemented in the General Structure Analysis System (GSAS) program.[22] The lattice constants, lithium occupancy, peak broadening, and corresponding anisotropy (where present) were fit assuming that the vibrational spectrum remained constant. To more accurately fit the zero-position of the Li_2O_2 diffraction pattern, peaks arising from aluminum mesh as well as carbon (carbon paper) were excluded from the fits.

Theoretical Calculations. First-principle calculations were performed using the Heyd–Scuseria–Ernzerhof (HSE) hybrid

functional[23,24] as implemented in the Vienna Ab Initio Simulation Package[25] (VASP) with the projector augmented wave (PAW) method,[26] because of its demonstrated ability to accurately describe the electronic properties of the Li_2O_2 system.[27] An energy cutoff of 800 eV was employed, and ionic relaxation was performed until a 10^{-4} eV per formula unit difference in energy was obtained.

Scanning Electron Microscopy (SEM). Electrodes were imaged after discharge (E-Li_2O_2) and at different stages during the charge process (E-Li_2O_2 and C-Li_2O_2). Electrodes were rinsed with dry tetrahydrofuran prior to analysis, and samples were prepared in an argon-filled glovebox, using a stainless steel holder as the substrate and double-sided carbon tape as the contact point between the electrode and the holder. Samples were transferred into the SEM (Zeiss LEO 1530 field-emission SEM) under anerobic conditions, and images were taken using an accelerating voltage of 5 kV.

■ RESULTS AND DISCUSSION

Dis(charging) of E-Li_2O_2. Operando X-ray diffraction patterns were collected on Li−O_2 cells run for a complete (dis)charge cycle at low and intermediate current densities of 25 and 50 $\mu A/cm^2$. The appearance and disappearance of the reflections in Figure 1a and Figure 1b belonging to Li_2O_2 (hereafter called E-Li_2O_2) prove its electrochemical formation and removal upon discharge and charge, respectively. Figure 1c shows a section of the diffraction patterns at the end of discharge for both current densities along with their Rietveld refinement. Using the Scherrer formula, we determined that smaller average crystallite sizes for E-Li_2O_2 are generated at a current density of 50 $\mu A/cm^2$ and larger crystallite sizes are formed at 25 $\mu A/cm^2$ (see Table 1) at the end of discharge.

Table 1. Lattice Parameters and Domain Sizes Obtained via Rietveld Refinement of Both Electrochemically Produced Li_2O_2 (End of Discharge) and Bulk Crystalline Li_2O_2.

type of Li_2O_2	lattice parameter		average domain size (nm)
	$a = b$ (Å)	c (Å)	
E-Li_2O_2 (25 $\mu A/cm^2$)	3.140	7.696	45.3 ± 0.9
E-Li_2O_2 (50 $\mu A/cm^2$)	3.143	7.781	26.3 ± 1.0
C-Li_2O_2	3.141	7.646	87.3 ± 1.4

This is in agreement with the simulations performed by Horstmann and co-workers on the rate dependent morphology of Li_2O_2.[14,28−30] From comparison of 25 $\mu A/cm^2$ (Figure 1c, upper panel) and 50 $\mu A/cm^2$ (Figure 1c, lower panel), the peaks corresponding to the (1 0 0) reflection are at the same angle in 2θ, whereas those corresponding to the (1 0 1) and (1 0 4) reflections are not. This is due to different c-lattice parameters for Li_2O_2 formed at the lower and higher current rates, of 7.696 and 7.781 Å, respectively (see Table 1). The value for the a-lattice parameter remained constant at ~3.141 ± 0.002 Å. From the work published by Adams et al.[14] it is known that the current density has a strong impact on the nature and morphology of the Li_2O_2 crystallites that are formed. The current density dependent mismatch in peak positions shown here has not been reported for ex situ measurements, possibly due to relaxation effects that occur during the time between discharge and the actual XRD measurement of the cathode. During this time, the c-lattice parameter can readily relax to values that are closer to the equilibrium value of bulk Li_2O_2 (7.64 Å). There was no significant variation or trend observed in the evolution of the lattice parameters as a function of discharge time. On the other hand, during charge there were subtle changes in the c-lattice parameter, especially visible for

the battery run at a low current density (Figure 2a). It remained constant for the first part of charge and showed a gradual increase in value toward the latter part of charge. These changes will be discussed below in correlation with the nature of the crystallites and the Li composition.

In order to fit the peak broadening, a variation on the pseudo-Voigt function with reflection asymmetry was implemented in GSAS.[22] Reflections appeared anisotropically broadened in the c-direction, with the magnitude being larger at lower current density. In GSAS, this was fitted by the microstrain broadening description given by Stephens,[33] resulting in nonzero values for coefficients corresponding to the anisotropic parameter in the c-direction (S_{004}). We cannot unequivocally distinguish between size and strain broadening given the limited 2θ data range. However, at lower discharge current densities, E-Li_2O_2 is known to form toroidal[34,35] aggregates, which consist of stacked Li_2O_2 crystalline platelets.[30] Published transmission electron micrographs of the Li_2O_2 toroids,[30] albeit those grown at a lower current density, show that the stacked platelike crystallites have large (0 0 0 1) crystal facets that grow plate by plate along the [0 0 1] direction. This results in anisotropic crystalline Li_2O_2 platelets that are approximately 10 nm in the c-direction and 400−600 nm in the ab-plane.[30] Assuming that our observed anisotropic broadening is solely due to size broadening, the X-ray diffraction pattern was further analyzed using the FULLPROF program[31,32] for which the Rietveld refinement includes an anisotropic size-broadening model based on spherical harmonics.[36] From this refinement we obtained apparent dimensions of 45.4 and 14.4 nm for the (1 0 0) and the (1 0 1) reflections, respectively. Note that diffraction is sensitive to the coherence length of the crystalline planes, which is in this case determined by the platelets and not the toroid shape. This translates into a disk-like crystallite plate shown in Figure 2d which is in agreement with that reported in literature.[30] The peak broadening and the anisotropic broadening as a function of charge time (Figure S2) both showed a small decrease toward the end of charge, suggesting an *increase* in average crystallite size, Figure 2b, as well a slightly more isotropic crystalline platelet shape toward the end of charge. The average increase in domain size shown in Figure 2b supports the model put forth by Radin and co-workers[19] proposing the initial decomposition of the smallest crystals, which should lead to an average narrowing of the reflections and therefore an increased average domain size. The limited decrease of the anisotropic broadening at the end of charge (Figure S2) indicates a small change in average particle shape, with the particles becoming more isotropic. In combination with the increase in isotropic domain size, this may indicate that thinner/flatter platelet crystallites are oxidized first. The limited change in average platelet dimensions, even at 80% state of charge, points toward a small active fraction of Li_2O_2 particles, and hence, a plate-by-plate-like oxidation. This is opposed to a larger active fraction, where an average decrease in crystallite size upon charge should lead to increased domain size broadening which is not observed here. It should be noted that diffraction is unable to probe the last stages of charge (corresponding to higher voltages) because of the low intensity of the reflections.

By following the evolution of peak intensity as a function of charge time for the (1 0 0) and (1 0 1) peaks of E-Li_2O_2 (Figure 1), we note that the growth of the peaks during the discharge is linear (Figure 1a), but a nonlinear decrease in peak intensity was observed during charge (Figure 1b). The
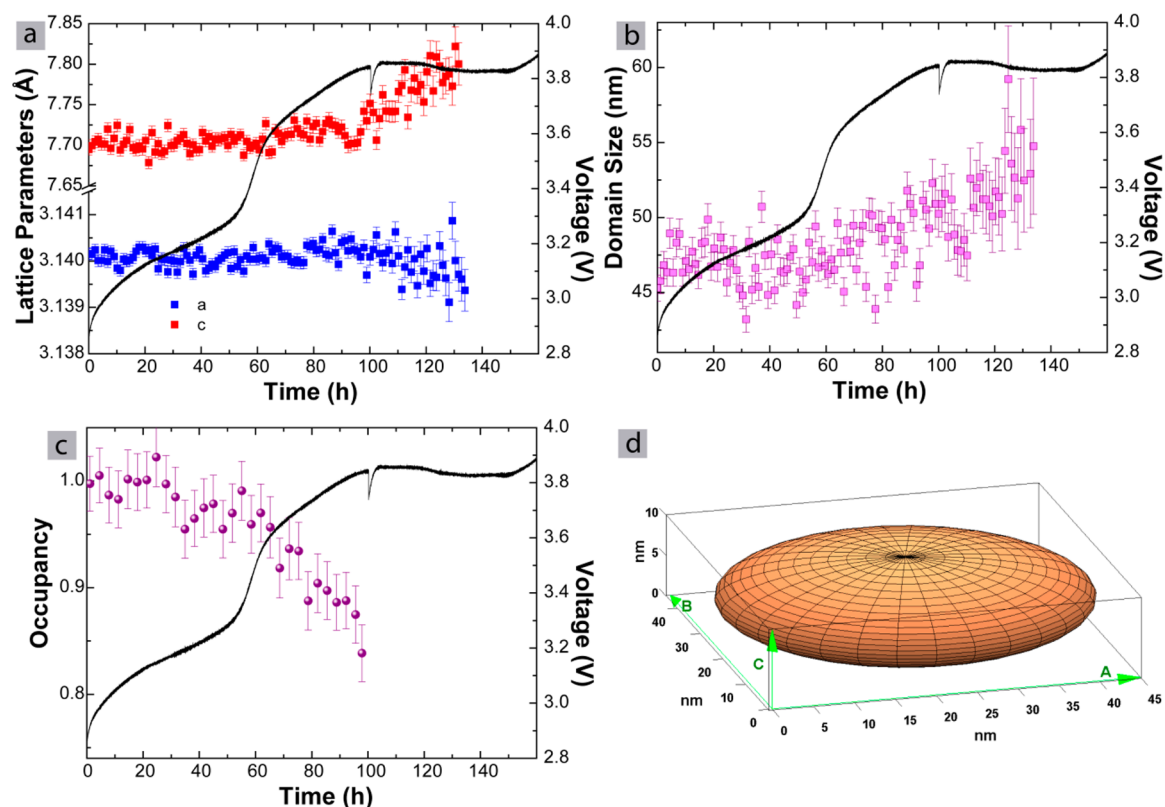
Figure 2. Galvanostatic charging of electrochemically formed Li$_2$O$_2$ (E-Li$_2$O$_2$) showing the evolution of the lattice parameters (a), average domain size (b), and average lithium occupancy (c) as a function of charge time. The corresponding voltage profiles as measured during charge have been illustrated in each graph. (d) Crystallite shape derived from the apparent coherence lengths obtained for the (1 0 0) and (1 0 1) reflections using FULLPROF.[31,32]
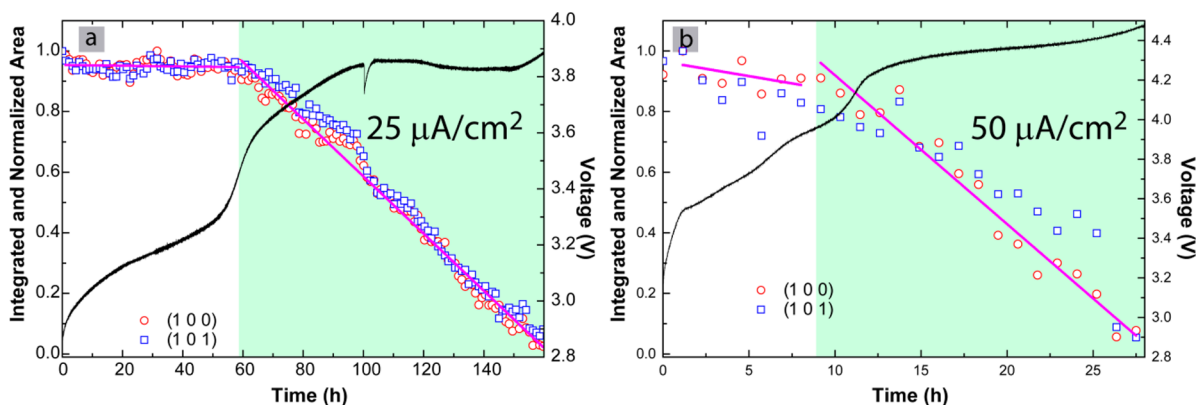

Figure 3. Galvanostatic charging of electrochemically formed Li$_2$O$_2$ (E-Li$_2$O$_2$). Integrated and normalized areas under the (1 0 0) and (1 0 1) peaks as a function of charge time have been plotted for current densities of (a) 25 and (b) 50 μA/cm^2, respectively. The pink lines indicate the linear fit of the points within the shaded or unshaded areas. The corresponding voltage profiles as measured have also been illustrated in each graph.

nonlinearity in the decay processes, as first reported by Lim and co-workers,[37] is observed irrespective of the current density used. From the integrated and normalized area under the (1 0 0) and (1 0 1) reflections as shown in Figure 3, we see that the decay takes place in two stages during charge, first slowly (static for a current density of 25 μA/cm^2) and then faster (linear). The decay in peak intensity (Figure 3a) coincides with an increase in voltage starting at 3.4 V and declines linearly over the second plateau up to a voltage of ~3.9 V. This is less obvious at the higher current densities (Figure 3b) because of the limited number of data points recorded. What is clear from both data sets, however, is that the decay of peak intensity

begins only *after* the first voltage plateau. The total lifetime of the peak intensity as seen through diffraction is also longer for discharge (Figure 1a, Figure 1b). The linear growth in peak intensity indicates a continuous uptake of O$_2$ to form E-Li$_2$O$_2$. This could occur (1) via a two-electron process (2Li$^+$ + O$_2$ + 2e$^-$ → Li$_2$O$_2$) or (2) via sequential one-electron processes[10,38] (Li$^+$ + O$_2$ + e$^-$ → LiO$_2$; LiO$_2$+Li$^+$ + e$^-$ → Li$_2$O$_2$) or (3) via a one-electron process to form LiO$_2$ followed by its disproportionation to form Li$_2$O$_2$[2,13,39] (Li$^+$ + O$_2$ + e$^-$ → LiO$_2$; 2LiO$_2$ → Li$_2$O$_2$ + O$_2$). At a constant reaction rate, the processes in mechanisms 2 and 3 must be rapid. During the first stage of charge the integrated area under the reflections is practically
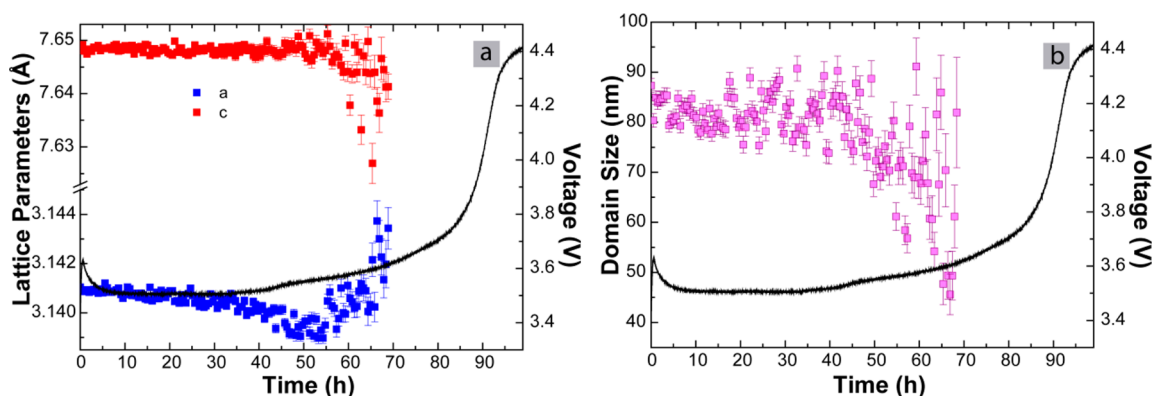
Figure 4. Galvanostatic charging of commercial Li_2O_2 (C-Li_2O_2). Evolution of (a) lattice parameters and (b) domain sizes as a function of charge time for C-Li_2O_2 electrodes obtained from Rietveld refined XRD patterns recorded operando at a current density of 25 $\mu A/cm^2$. The corresponding voltage profiles as measured have also been illustrated in each graph.

constant, indicating preferential decomposition of surface LiO_2 species and/or of any *amorphous* Li_2O_2 component that may be present in the lower voltage regime (2.8−3.4 V).[9,15−17,40] The second stage is characterized by a linear decrease in integrated area under the reflections, indicating the complete oxidation of E-Li_2O_2 grains and evolution of O_2. Despite the relative stability of TEGDME toward peroxide, it has already been reported by some authors[39] that small amounts of Li_2CO_3 are formed in the initial part of the charge process, which has been attributed to the possible reaction of highly active nascent O_2^* that is released or due to the reactivity of the substoichiometric $Li_{2−x}O_2$ intermediates. These reactions could be responsible for the disparity in peak decay rates observed for charge vis-à-vis discharge (Figure 1a, Figure 1b).

From the Rietveld refinement of the diffraction data during charge, a clear evolution of the Li-occupancy was observed as a function of charge duration (Figure 2c). Obtaining Li-occupancies from X-ray diffraction is usually quite difficult because of the low atomic number of Li compared to the other typically heavier elements present. However, in Li_2O_2, the reflections are very sensitive to both oxygen and lithium occupancies, and thus they can be easily determined. The results show there is a gradual decrease in the lithium occupancy from ~3.2 V that begins slightly before the decline in the diffraction peak intensity (Figure 3a). This indicates that the decomposition of E-Li_2O_2 must take place via substoichiometric E-$Li_{2−x}O_2$ intermediates and that during charge, the system becomes on average increasingly lithium deficient. Given the predicted decrease in the c-lattice parameter for Li substoichiometric $Li_{2−x}O_2$ by DFT calculations,[41] this poses a contradiction to the almost constant c-lattice parameter on charge in Figure 2c. To investigate the dependence of the lattice parameters change on lithium vacancies in more detail, two similar DFT calculations were performed on a 2 × 2 × 1 supercell of Li_2O_2 by removing one lithium from either of the two crystallographically distinct lithium sites in the structure (Li1 and Li2), both resulting in a 0.93 occupancy. On relaxation, both structures showed virtually no decrease in the a-lattice parameter upon lithium removal (i.e., <1%). For removal of the lithium atom between the O and O positions (Li2, Figure S3), a noticeable decrease (1.6%) in the c-lattice parameter was observed, compared to the removal of the interlayer lithium atom (Li1), which shows virtually no change in the c-lattice parameter (<0.15%, Table S1). Hence, the creation of lithium vacancies observed in Figure 2c is most

likely due to vacancies on the Li1 site consistent with the absence of a significant change in lattice parameters, at least for dilute vacancy concentrations. This is reasonable because the energy required to create a lithium vacancy at the Li2 position is higher than at Li1.[42] In addition, the small increase observed in the c-lattice parameter as a function of charge time may be correlated to the disintegration of the toroid shaped secondary particles. By stripping of primary platelet crystallites from the toroids, additional low energy (0 0 0 1) surfaces of the platelets would be exposed. For nanostructured metal oxides, this typically leads to an expansion of lattice parameters[43] attributed to an increase in the surface energy due to larger exposed surfaces that is manifested at smaller crystallite sizes. A widely studied example of this phenomenon is CeO_2, which exhibits an increase in the fraction of surface oxygen in the form of superoxide at nanocrystallite dimensions.[44] Therefore, this increase in the c-lattice parameter could be indicative of more exposed surfaces in E-Li_2O_2 as the state of charge progresses.

Charging of C-Li_2O_2. To probe the oxygen evolution mechanism, charge-only operando XRD experiments were performed using electrodes preloaded with bulk, crystalline commercial Li_2O_2 (hereafter called C-Li_2O_2). As this material has a higher degree of crystallinity (Figure S4) than that formed upon electrochemical reduction, higher X-ray diffraction peak intensities result. This allows for better statistics and/or time resolution of the measurement during charge. In addition, the different nature of these particles may provide insight in the charge mechanism. Experiments were performed using current densities of 25 and 50 $\mu A/cm^2$, comparable to the E-Li_2O_2 experiments. The sharp voltage rise and drop at the beginning of the voltage profiles (see Figure 4) is due to a reaction between carbon and Li_2O_2 at their interface and is referred to as the "activation process".[45] The pristine cathode diffraction pattern, measured before charging, along with its Rietveld refinement is given in the Supporting Information (Figure S5). Only peaks from Li_2O_2 are visible indicating that any LiOH impurities[46] present are obviously amorphous and should not influence the monitoring of crystalline Li_2O_2 oxidation. From this, the initial lattice parameters of Li_2O_2 were obtained; a = 3.141 Å and c = 7.646 Å (Table 1). At 50 $\mu A/cm^2$, the a- and c-lattice parameters remained relatively constant until higher charge overpotentials were reached (after the plateau at ~3.7 V, Figure S6) at which point the a-parameter increased. The opposite trend was observed for the c-parameter. At a lower current density (25 $\mu A/cm^2$, Figure 4a), more complex

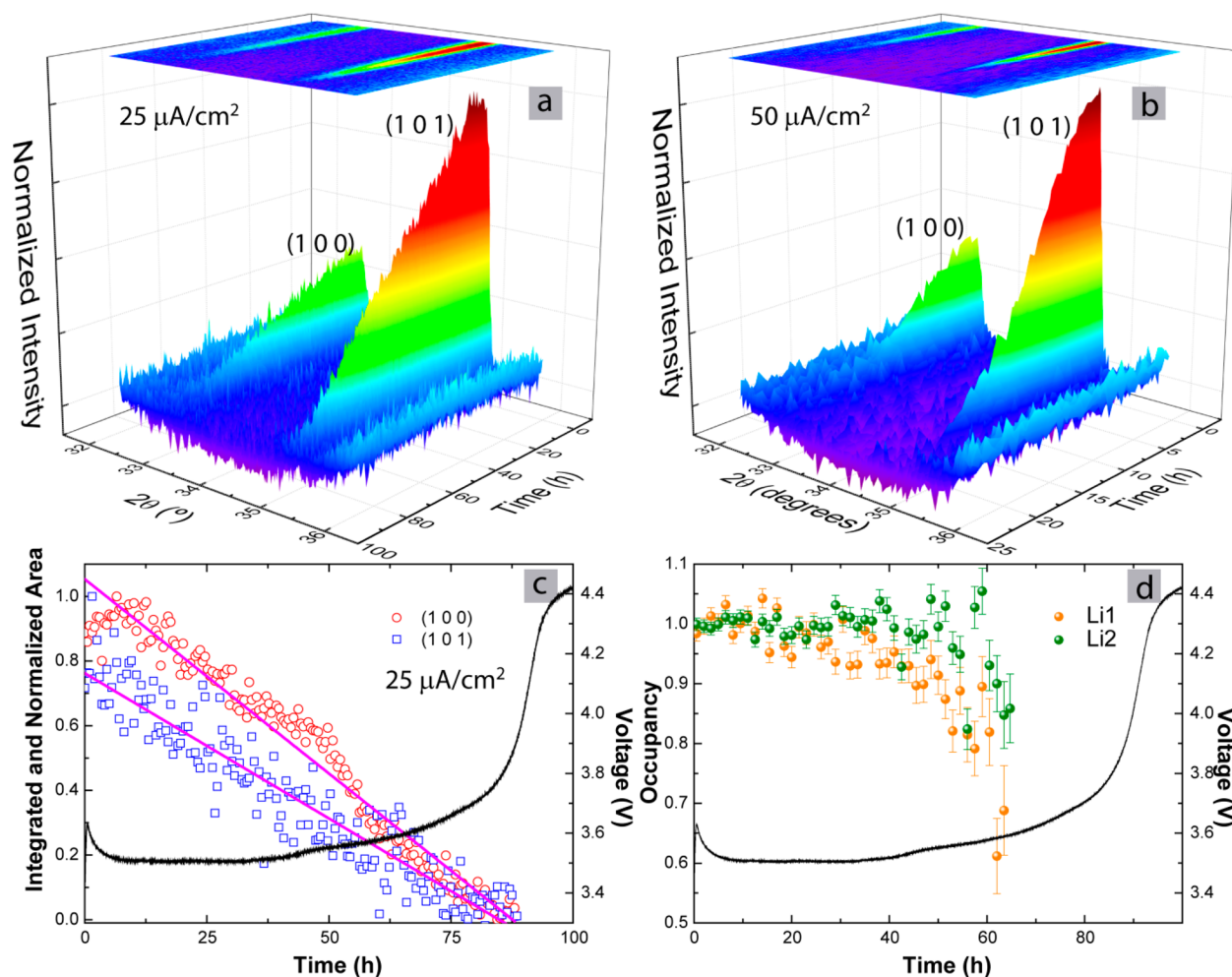**Figure 5.** Galvanostatic charging of commercial Li_2O_2 (C-Li_2O_2). (a, b) Three dimensional plots of the XRD patterns in the 2θ region of $32-36°$, recorded in situ as a function of time during charge with constant currents of 25 and 50 $\mu A/cm^2$, respectively. Peaks corresponding to the (1 0 0) and (1 0 1) reflections of C-Li_2O_2 are visible. (c) Integrated and normalized area under the (1 0 0) and (1 0 1) peaks as a function of charge time recorded with a current density of 25 $\mu A/cm^2$. The pink lines represent a linear fit of the intensities of the (1 0 0) and (1 0 1) reflections. (d) Evolution of the lithium occupancy for the Li1 and Li2 sites obtained via Rietveld refinement of the diffraction patterns as a function of charge time recorded with a current density of 25 $\mu A/cm^2$. Charge voltage profiles for both are shown.

behavior was observed. Initially, both the a and c-parameters remained constant, followed by a gradual decrease in a. A small shift in the discharge profile to higher voltage is accompanied by the sharp onset of an increase in the a-parameter accompanied by the opposite in c. No anisotropic broadening was observed, indicating an isotropic crystallite shape (Figure S4), in contrast to the platelike Li_2O_2 crystallites formed electrochemically. The evolution of domain sizes (Figure 4b) obtained from the peak widths remained relatively constant to about the 50 h point, after which the average domain size continuously decreased. Values for the lattice parameters and domain sizes beyond 70 h of charge are unreliable because of very low peak intensities.

For the charge at 25 $\mu A/cm^2$, the increase in the charge overpotential and a-parameter along with the decrease in the c-parameter at the 50-h mark of charge suggests the emergence of a dominant lithium substoichiometric $Li_{2-x}O_2$ phase (Figure 4a). Theoretical calculations[18] have shown that bulk species (tending toward LiO_2) would have an increasingly smaller c-parameter. Most likely, the lower surface to bulk ratio of the larger isotropic C-Li_2O_2 crystallites does not introduce the competing increase in c observed for the oxidation of E-Li_2O_2.

Hence, the decrease in the c-parameter appears to be directly related to lithium substoichiometry. The evolution of domain sizes for C-Li_2O_2 determined from the isotropic broadening over charge as shown in Figure 4b, assuming the absence of strain, remains practically constant in the plateau (up to 50 h of charge) after which there is a continuous decrease with higher voltage. Although this could indicate a two-stage transformation mechanism, this appears unlikely given the linear decrease in X-ray reflections shown in Figure 5a. In addition, the constant oxygen evolution measured by online electrochemical mass spectrometry (OEMS), Figure S8, supports a single stage oxidation process for C-Li_2O_2. In this context, the evolution of the average domain size in Figure 4b most likely indicates a small oxidizing fraction of Li_2O_2 for which the domain size reduces due to disintegration. Such a small actively transforming fraction will have negligible impact on the average domain size at the early stage of charge. At the end of charge the same amount of actively transforming material will constitute a relatively larger fraction of the remaining Li_2O_2, resulting in an average decrease in domain size at the end of charge.
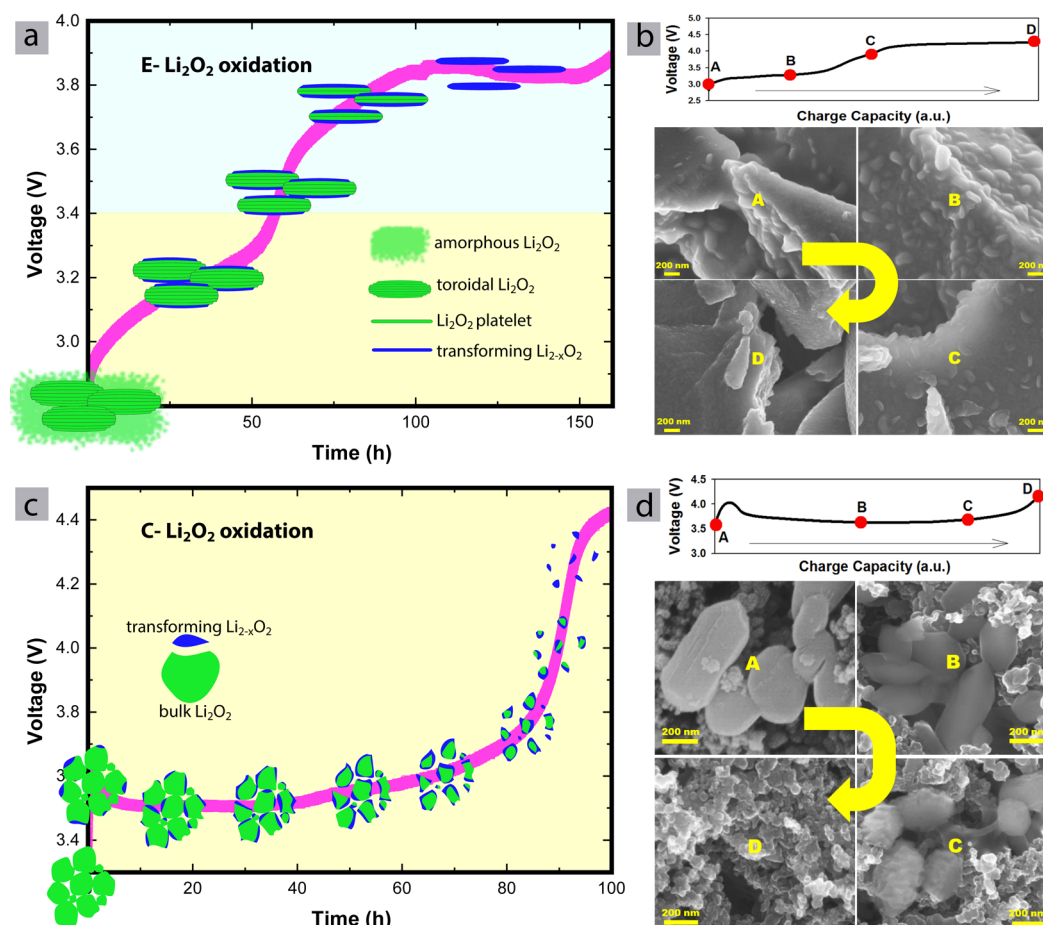
Figure 6. Cartoon showing the mechanism of (a) E-Li_2O_2 and (c) C-Li_2O_2 oxidation during the charge process as determined from X-ray diffraction. Scanning electron microscopy images (SEM) recorded at different stages of oxidation of E-Li_2O_2 and C-Li_2O_2 are depicted in panels (b) and (d), respectively.

Although the decline in diffracted intensity during charge of the C-Li_2O_2 cathodes is on average linear, as is evident from Figure 5a, the individual decline of the (1 0 0) and (1 0 1) reflections shows a marked difference as observed from the integrated area under the (1 0 0) and (1 0 1) peaks as a function of charge duration shown in Figure 5c. Factors that commonly affect the relative intensities between reflections include changes in atomic positions as well as in their occupancies. Lithium occupies two distinct crystallographic sites in Li_2O_2: the interlayer Li1 position and the Li2 position next to the oxygen dumbbell, as shown in the Supporting Information (Figure S3). If both sites are occupied, the ratio of the normalized and integrated intensity under the (1 0 0) and (1 0 1) peaks should be 1, i.e., (1 0 0):(1 0 1) = 1. On the other hand, an isostructural LiO_2 system constructed with only Li1 missing gives rise to diffraction patterns with (1 0 0):(1 0 1) > 1 and a system with Li2 absent gives rise to diffraction patterns with (1 0 0):(1 0 1) < 1 (simulated diffraction patterns are given in Figure S3). Therefore, Figure 5c indicates preferential Li1 vacancies occurring upon charge. This was quantified by Rietveld refinement of both Li1 and Li2 occupancies of the C-Li_2O_2 diffraction data as a function of charge time (Figure 5d). The Li occupancy of the Li2 site remains constant (close to 1) until the 50 h mark of charge, whereas the occupancy at the Li1 site shows a gradual decrease, creating Li1 vacancies, from the onset of charge. After 50 h of charge Li2 vacancies also appear to be created, consistent with evolution of the integrated

intensity of the (1 0 0) reflection in Figure 5c. Consistent with the DFT calculations discussed above and the reported lower energy of Li1 vacancy formation, the operando diffraction of C-Li_2O_2 indicates preferential formation of Li1 vacancies at the onset of charge. This again points toward oxidation through a Li-deficient solid solution reaction. The increase in average vacancy concentration observed at the end of charge in Figure 5d is most likely the consequence of the small actively oxidizing $Li_{2-x}O_2$ fraction, the properties of which become more apparent at the end of charge when almost no passive Li_2O_2 is present.

Charge Mechanism. From the data extracted from the operando diffraction patterns measured during the charge of E-Li_2O_2, two oxidation stages can be distinguished (Figure 6a). During the first stage, amorphous Li_2O_2 and the smallest crystallites oxidize at the low voltage plateau between 2.8 and 3.4 V. This is supported by the absence of the change in diffracted intensity and absence of any evolution in the parameters obtained from Rietveld refinement, with the exception of the Li-occupancy. This indicates that some Li vacancies are created, resulting in a small fraction of substoichiometric $Li_{2-x}O_2$. During the second stage, in the voltage range 3.4–3.9 V, a continuous drop in the XRD peak intensity is observed, accompanied by a continuing decrease in the Li-occupancy. This indicates that the oxidation is solid solution driven, proceeding in two steps, i.e., (1) $Li_2O_2 \rightarrow Li_{2-x}O_2 + xLi^+ + xe^-$ and (2) $Li_{2-x}O_2 \rightarrow (2-x)Li^+ + (2-$

x)e$^-$ + O$_2$. In addition, the decrease in both isotropic and anisotropic peak broadening indicates that the smallest and thinnest platelet crystallites are oxidized preferentially, leaving the largest platelets at the end of charge. This model is further validated by scanning electron microscopy (SEM) images recorded at different states of charge of E-Li$_2$O$_2$ (dis)charged at a current density of 25 μA/cm^2 as shown in Figure 6b. In image A, which represents the state of the cathode at the end of discharge, toroids of Li$_2$O$_2$ are covered by an amorphous lithium suboxide blanket. At ~25% of charge (image B) more toroids become visible, indicating that the lithium suboxide blanket is oxidized first. By ~50% of charge (image C) the amorphous blanket has completely disappeared and the toroids are noticeably thinner. Image C, measured at the end of charge, shows that no Li$_2$O$_2$ remains, either amorphous or toroidal.

Thereby, the operando diffraction study supports both the charge model via solid-solution compositions brought forward by Kang et al.[18] and the preferable decomposition of the smallest crystallites brought forward by Radin et al.[19,20,40] In addition, the limited change in average crystallite dimensions at the end of charge indicates that a plate-by-plate-like oxidation process occurs. This "two-stage" oxidation mechanism for E-Li$_2$O$_2$ is slightly complicated by electrochemical decomposition which occurs during discharge and the subsequent oxidation of these side products during charge.[47,48] We note that the rise in voltage from the amorphous region (2.8–3.4 V) to the second plateau can be influenced by these side products, yet the observed diffraction data for Li$_2$O$_2$ should not be affected. Although lithium carbonate is not oxidized below 4 V, lithium formate can be oxidized around 3.8 V,[49] which most likely impacts the upper voltage plateau.

The operando diffraction of the chemical C-Li$_2$O$_2$ supports a single oxidation stage via a small actively transforming fraction (Figure 6c). The continuous decrease in peak intensity of the (1 0 0) and the (1 0 1) reflections indicates the continuous decomposition of C-Li$_2$O$_2$ throughout the charge process (Figure 5a). This is consistent with operando mass spectrometry measurements[46,50,51] that have been performed during charge with preloaded cathodes, which report a continuous evolution of O$_2$ also during the initial part of charge. Noteworthy is the delay in oxygen evolution observed here (Figure S8, red dashed line) until this overpotential is overcome. This, along with the small amount of CO$_2$ evolved during this initial stage of charge in the preloaded (C-Li$_2$O$_2$) electrodes, indicates a chemical reaction between the Li$_2$O$_2$ and carbon to form an oxidized carbon interface. After the overpotential is surmounted, a single-stage oxidation process dictates a constant O$_2$ evolution rate until the end of charge. The small amount of CO$_2$ that is produced at the end of charge is presumed to be due to the oxidation of electrolyte decomposition products (lithium formate, carbonate, etc.) as the voltage increases. These are formed at the reactive Li$_{2-x}$O$_2$ surface throughout the charge process.

The evolution of the Li1 occupancy (Figure 5d, reflecting the Li deficiency) and the isotropic broadening of the reflections (indicating a decrease in average crystallite size, Figure 4b) both show a change that increases with the state of charge. This can be explained by a small actively oxidizing C-Li$_2$O$_2$ fraction. This fraction is most likely limited to the surface regions of the larger peroxide crystallites at the onset of charge, resulting in no discernible changes in broadening of the diffraction peaks. This is confirmed by additional SEM images (Figure 6d) measured on C-Li$_2$O$_2$ oxidized to different states of charge. In image C at

~75% charge, there is clear evidence of a decrease in particle size as well as surface oxidation. As the state-of charge progresses, the actively transforming C-Li$_{2-x}$O$_2$ fraction relatively increases relative to the untransformed C-Li$_2$O$_2$ that remains and the Li1 vacancies become apparent in the average Li occupancies. In this case, the decrease in c-lattice parameter indicates that the C-Li$_2$O$_2$ is much less exposed compared to E-Li$_2$O$_2$. The strong current rate dependence for the charge process supports the oxidation occurring preferentially at the outer surface of the crystallites for both C-Li$_2$O$_2$ and E-Li$_2$O$_2$ (as depicted in Figure 6). In the work of Adams et al.,[14] the overall charge profiles were lowered in voltage with decreasing charge current density when electrodes were discharged at the same current density (E-Li$_2$O$_2$). The same effect is seen here for C-Li$_2$O$_2$, when examining the voltage plateaus at different current densities. In Figures 4/5, S6/S7, and S8, the main voltage plateaus occur at approximately 3.6, 3.8, and 4.0 V, when current densities of 25, 50, and 75 μA/cm^2 are used, respectively. This current/voltage relation can be explained by the necessity of electron transport from the carbon support through the insulating Li$_2$O$_2$ to the active oxidizing surface fraction (Li$_{2-x}$O$_2$).

CONCLUSIONS

We combine operando X-ray diffraction, Rietveld refinement, OEMS, and theoretical calculations to characterize the different stages of Li$_2$O$_2$ oxidation during the charge reaction in a Li−O$_2$ cell for both electrochemically and bulk crystalline Li$_2$O$_2$ (E-Li$_2$O$_2$ and C-Li$_2$O$_2$, respectively). Different oxidation processes were observed for E-Li$_2$O$_2$ and C-Li$_2$O$_2$ associated with the differences in their nature. For electrochemically formed Li$_2$O$_2$ we propose a two-stage oxidation. At low potentials this involves the decay of amorphous Li$_2$O$_2$, whereas at higher potentials, crystalline Li$_2$O$_2$ is decomposed via a small actively transforming fraction that evolves oxygen via a Li deficient solid-solution reaction. This preferentially starts with the smallest crystallites. Rietveld refinement of the diffraction data measured during charge additionally reveals a very small increase in the c-lattice parameter as a function of charge duration, which can be correlated to an increase in surface energy due to more exposed E-Li$_2$O$_2$ surfaces: the consequence of removing the crystallite platelets that build up the toroidal aggregates. DFT calculations indicate that dilute Li deficiencies do not significantly affect the lattice parameters when they occur on the energetically preferred interlayer Li position. This allows for a small increase in the c-lattice parameter concomitant with a decrease in lithium occupancy, i.e., more exposed surfaces having higher surface energies (hence leading to slightly larger lattice parameters). For bulk crystalline Li$_2$O$_2$ with an isotropic crystallite shape and larger crystallite dimensions, we propose a single stage oxidation on the basis of the XRD data. The observation of substoichiometric Li$_{2-x}$O$_2$ at the early stage of oxidation and the gradual decreasing average crystallite size suggests a small active fraction that also evolves oxygen via a Li deficient solid solution reaction. However, in this case the oxidation process gradually consumes the larger C-Li$_2$O$_2$ crystallites. Detailed refinement of the C-Li$_2$O$_2$ patterns indicates that substoichiometric Li$_{2-x}$O$_2$ is created by the formation of vacancies on the interlayer Li1 positions and in particular at the early stages of oxidation. These findings not only reveal the fundamental nature of the charge reaction in Li−air batteries but also show the impact that the nature of the lithium peroxide (size, shape, and

16342

dx.doi.org/10.1021/ja508794r | J. Am. Chem. Soc. 2014, 136, 16335−16344

crystallinity) has on the oxidation mechanism. Controlling this process may be the key to high performance Li−air batteries.

■ ASSOCIATED CONTENT

Ⓢ Supporting Information

Table with the lattice parameters determined from first principle calculations and supplementary figures. This material is available free of charge via the Internet at http://pubs.acs.org.

■ AUTHOR INFORMATION

Corresponding Authors
lfnazar@uwaterloo.ca
m.wagemaker@tudelft.nl

Notes
The authors declare no competing financial interest.

■ ACKNOWLEDGMENTS

■ REFERENCES

(1) Abraham, K. M.; Jiang, Z. *J. Electrochem. Soc.* **1996**, *143*, 1.
(2) Peng, Z.; Freunberger, S. A.; Chen, Y.; Bruce, P. G. *Science* **2012**, *337*, 563.
(3) Bruce, P. G.; Freunberger, S. A.; Hardwick, L. J.; Tarascon, J. M. *Nat. Mater.* **2012**, *11*, 19.
(4) Black, R.; Adams, B.; Nazar, L. F. *Adv. Energy Mater.* **2012**, *2*, 801.
(5) Christensen, J.; Albertus, P.; Sanchez-Carrera, R. S.; Lohmann, T.; Kozinsky, B.; Liedtke, R.; Ahmed, J.; Kojic, A. *J. Electrochem. Soc.* **2012**, *159*, R1.
(6) Garcia-Araez, N.; Novák, P. *J. Solid State Electrochem.* **2013**, *17*, 1793.
(7) Lu, Y. C.; Gallant, B. M.; Kwabi, D. G.; Harding, J. R.; Mitchell, R. R.; Whittingham, M. S.; Shao-Horn, Y. *Energy Environ. Sci.* **2013**, *6*, 750.
(8) Lee, J. H.; Black, R.; Popov, G.; Pomerantseva, E.; Nan, F.; Botton, G. A.; Nazar, L. F. *Energy Environ. Sci.* **2012**, *5*, 9558.
(9) McCloskey, B. D.; Bethune, D. S.; Shelby, R. M.; Girishkumar, G.; Luntz, A. C. *J. Phys. Chem. Lett.* **2011**, *2*, 1161.
(10) McCloskey, B. D.; Scheffler, R.; Speidel, A.; Girishkumar, G.; Luntz, A. C. *J. Phys. Chem. C* **2012**, *116*, 23897.
(11) McCloskey, B. D.; Speidel, A.; Scheffler, R.; Miller, D. C.; Viswanathan, V.; Hummelshøj, J. S.; Nørskov, J. K.; Luntz, A. C. *J. Phys. Chem. Lett.* **2012**, *3*, 997.
(12) Gowda, S. R.; Brunet, A.; Wallraff, G. M.; McCloskey, B. D. *J. Phys. Chem. Lett.* **2013**, *4*, 276.
(13) Laoire, C. O.; Mukerjee, S.; Abraham, K. M.; Plichta, E. J.; Hendrickson, M. A. *J. Phys. Chem. C* **2010**, *114*, 9178.
(14) Adams, B. D.; Radtke, C.; Black, R.; Trudeau, M. L.; Zaghib, K.; Nazar, L. F. *Energy Environ. Sci.* **2013**, *6*, 1772.
(15) Gallant, B. M.; Kwabi, D. G.; Mitchell, R. R.; Zhou, J.; Thompson, C. V.; Shao-Horn, Y. *Energy Environ. Sci.* **2013**, *6*, 2518.
(16) Yang, J.; Zhai, D.; Wang, H. H.; Lau, K. C.; Schlueter, J. A.; Du, P.; Myers, D. J.; Sun, Y. K.; Curtiss, L. A.; Amine, K. *Phys. Chem. Chem. Phys.* **2013**, *15*, 3764.
(17) Zhai, D.; Wang, H. H.; Yang, J.; Lau, K. C.; Li, K.; Amine, K.; Curtiss, L. A. *J. Am. Chem. Soc.* **2013**, *135*, 15364.
(18) Kang, S.; Mo, Y.; Ong, S. P.; Ceder, G. *Chem. Mater.* **2013**, *25*, 3328.
(19) Radin, M. D.; Siegel, D. J. *Energy Environ. Sci.* **2013**, *6*, 2370.
(20) Lu, J.; Lei, Y.; Lau, K. C.; Luo, X.; Du, P.; Wen, J.; Assary, R. S.; Das, U.; Miller, D. J.; Elam, J. W.; Albishri, H. M.; El-Hady, D. A.; Sun, Y.-K.; Curtiss, L. A.; Amine, K. *Nat. Commun.* **2013**, *4*, 2383.
(21) Garsuch, R. R.; Le, D. B.; Garsuch, A.; Li, J.; Wang, S.; Farooq, A.; Dahn, J. R. *J. Electrochem. Soc.* **2008**, *155*, A721.
(22) Larson, A. C.; Von Dreele, R. B. *General Structure Analysis System (GSAS)*; Los Alamos National Laboratory: Los Alamos, NM, 2004.
(23) Heyd, J.; Scuseria, G. E.; Ernzerhof, M. *J. Chem. Phys.* **2003**, *118*, 8207.
(24) Heyd, J.; Scuseria, G. E.; Ernzerhof, M. *J. Chem. Phys.* **2006**, *124*, 219906.
(25) Kresse, G.; Furthmuller, J. *Comput. Mater. Sci.* **1996**, *6*, 15.
(26) Kresse, G.; Joubert, D. *Phys. Rev. B* **1999**, *59*, 1758.
(27) Ong, S. P.; Mo, Y.; Ceder, G. *Phys. Rev. B: Condens. Matter Mater. Phys.* **2012**, *85*, 081105.
(28) Gallant, B. M.; Mitchell, R. R.; Kwabi, D. G.; Zhou, J.; Zuin, L.; Thompson, C. V.; Shao-Horn, Y. *J. Phys. Chem. C* **2012**, *116*, 20800.
(29) Horstmann, B.; Gallant, B.; Mitchell, R.; Bessler, W. G.; Shao-Horn, Y.; Bazant, M. Z. *J. Phys. Chem. Lett.* **2013**, *4*, 4217.
(30) Mitchell, R. R.; Gallant, B. M.; Shao-Horn, Y.; Thompson, C. V. *J. Phys. Chem. Lett.* **2013**, *4*, 1060.
(31) Rodríguez-Carvajal, J. *Phys. B (Amsterdam, Neth.)* **1993**, *192*, 55.
(32) Roisnel, T.; Rodríguez-Carvajal, J. *Proceedings of the Seventh European Powder Diffraction Conference*, Barcelona, Spain, May 20−23, 2000; Delhez, R., Mittemeijer, E. J., Eds.; Scitec Publications: Zurich, Switzerland, 2001; p 118.
(33) Stephens, P. W. *J. Appl. Crystallogr.* **1999**, *32*, 281.
(34) Black, R.; Oh, S. H.; Lee, J. H.; Yim, T.; Adams, B.; Nazar, L. F. *J. Am. Chem. Soc.* **2012**, *134*, 2902.
(35) Mitchell, R. R.; Gallant, B. M.; Thompson, C. V.; Shao-Horn, Y. *Energy Environ. Sci.* **2011**, *4*, 2952.
(36) Popa, N. C. *J. Appl. Crystallogr.* **1998**, *31*, 176.
(37) Lim, H.; Yilmaz, E.; Byon, H. R. *J. Phys. Chem. Lett.* **2012**, *3*, 3210.
(38) Hummelshøj, J. S.; Blomqvist, J.; Datta, S.; Vegge, T.; Rossmeisl, J.; Thygesen, K. S.; Luntz, A. C.; Jacobsen, K. W.; Nørskov, J. K. *J. Chem. Phys.* **2010**, *132*.
(39) Black, R.; Lee, J. H.; Adams, B.; Mims, C. A.; Nazar, L. F. *Angew. Chem., Int. Ed.* **2013**, *52*, 392.
(40) Tian, F.; Radin, M. D.; Siegel, D. J. *Chem. Mater.* **2014**, *26*, 2952.
(41) Hohenberg, P.; Kohn, W. *Phys. Rev.* **1964**, *136*, B864.
(42) Varley, J. B.; Viswanathan, V.; Nørskov, J. K.; Luntz, A. C. *Energy Environ. Sci.* **2014**, *7*, 720.
(43) Diehm, P. M.; Ágoston, P.; Albe, K. *ChemPhysChem* **2012**, *13*, 2443.
(44) Xu, J.; Harmer, J.; Li, G.; Chapman, T.; Collier, P.; Longworth, S.; Tsang, S. C. *Chem. Commun.* **2010**, *46*, 1887.
(45) Meini, S.; Solchenbach, S.; Piana, M.; Gasteiger, H. A. *J. Electrochem. Soc.* **2014**, *161*, A1306.
(46) Meini, S.; Tsiouvaras, N.; Schwenke, K. U.; Piana, M.; Beyer, H.; Lange, L.; Gasteiger, H. A. *Phys. Chem. Chem. Phys.* **2013**, *15*, 11478.
(47) McCloskey, B. D.; Valery, A.; Luntz, A. C.; Gowda, S. R.; Wallraff, G. M.; Garcia, J. M.; Mori, T.; Krupp, L. E. *J. Phys. Chem. Lett.* **2013**, *4*, 2989.
(48) Adams, B. D.; Black, R.; Williams, Z.; Fernandes, R.; Cuisinier, M.; Jaemstorp Berg, E.; Novak, P.; Murphy, G. K.; Nazar, L. F. *Adv. Energy Mater.* **2014**, DOI: 10.1002/aenm.201400867.
(49) Freunberger, S. A.; Chen, Y.; Peng, Z.; Griffin, J. M.; Hardwick, L. J.; Bardé, F.; Novák, P.; Bruce, P. G. *J. Am. Chem. Soc.* **2011**, *133*, 8040.

(50) Xu, W.; Viswanathan, V. V.; Wang, D.; Towne, S. A.; Xiao, J.; Nie, Z.; Hu, D.; Zhang, J. G. *J. Power Sources* **2011**, *196*, 3894.

(51) Beyer, H.; Meini, S.; Tsiouvaras, N.; Piana, M.; Gasteiger, H. A. *Phys. Chem. Chem. Phys.* **2013**, *15*, 11025.